RSC Advances

PAPER

View Article Online
View Journal | View Issue

Cite this: *RSC Adv.*, 2025, **15**, 33374

Design of Ni-modified ZnSe nanostructures embedded in rGO for efficient supercapacitor electrodes

Sana Ullah Asif, *[a] Abdul Shakoor,[b] Bushra Asghar,[c] Abdul Waheed,[d] Abdullah K. Alanazi,[e] Muhammad Ehsan Mazhar, *[c] Shahid Atiq, [b] Muhammad Yahya Haroon,[b] Sadia,[b] Abdul Qayyum,[f] Waseem Abbas,[c] Zainab Bano[g] and Farooq Ahmad *[b]

Energy crises have prompted researchers to develop new electrode materials for efficient energy storage, leading to the creation of effective energy storage devices. Therefore, this study introduces Ni-doped ZnSe/rGO-based materials fabricated through a hydrothermal synthesis method, which demonstrated enhanced electrical and electrochemical performance. X-ray diffraction (XRD) analysis revealed an increase in the crystallite size from 49.72 nm to 96.74 nm, accompanied by a corresponding growth in the particle size, which can be attributed to the incorporation of Ni and rGO as substituents. The electrochemical characterization of all fabricated electrodes indicated that the best-performing $Zn_{0.90}Ni_{0.10}Se$/rGO composite achieved a high specific capacitance of 1920.20 F g^{-1} at 5 mV s^{-1}, significantly surpassing that of pure ZnSe (346.8 F g^{-1}), as determined from CV measurements. Additionally, the $Zn_{0.90}Ni_{0.10}Se$/rGO electrode demonstrated excellent cycling stability (90.85% capacitance retention after 10 000 cycles), a high power density of 3500 W kg^{-1} at a current density of 7 A g^{-1}, and an energy density of 83.81 Wh kg^{-1} at a current density of 1 A g^{-1}, with a storage capability of 1058.75 F g^{-1}. The combined effect of Ni and rGO doping in the composites resulted in a notable reduction in series and charge transfer resistances. Under optimal conditions, it exhibited excellent electrochemical performance, as indicated by good ionic conductivity (0.037 S cm^{-1}), the highest transference number for cations (0.90), and a rate constant of 1.42 × 10^{-8} cm s^{-1} at an exchange current density of 0.00137 A g^{-1}, as well as a diffusion coefficient of 8.03 × 10^{-13} m^2 s^{-1}, suggesting enhanced ion transport characteristics. These promising attributes of $Zn_{0.90}Ni_{0.10}Se$/rGO strongly demonstrate it as an ideal electrode material for advanced energy storage applications.

Received 17th July 2025
Accepted 27th August 2025

DOI: 10.1039/d5ra05161d

rsc.li/rsc-advances

1. Introduction

The rapid development of modern industrial society has led to severe environmental pollution and has triggered an energy crisis.[1,2] These global concerns, including climate change, global warming, and fossil fuel depletion, have intensified interest in developing advanced energy conversion technologies as promising pathways for producing higher-value fuels.[3] As a result, the intermittent nature of sustainable energy sources, such as wind, tidal, and solar power, has made the development of new, large-scale energy storage devices with improved performance a challenging research problem.[4]

The energy has been significantly affected by globalization, which involves saving extra energy and reusing it when resources are scarce. In this regard, several varieties of energy storage devices are available, including batteries, fuel cells, typical capacitors, and supercapacitors (SCs), which differ in their energy storage capabilities. These can be differentiated by their energy and power densities, which can help mitigate energy storage issues. Usually, SCs are the fundamental parts of energy storage systems. They are a key component for storing electrical energy in the microfarad range. Their anode and cathode remain the same, making them similar to batteries in that aspect. However, batteries provide high energy densities, while SCs deliver high power densities by storing charge at the electrode/electrolyte interface.[5] Their high power density, rapid

[a]*Department of Physics, Qilu Institute of Technology, Jinan 250200, Shandong, P. R. China. E-mail: sanaullahasif@gmail.com*

[b]*Centre of Excellence in Solid State Physics, University of the Punjab, Lahore, 54590, Pakistan. E-mail: ahmadfarooq1999@gmail.com*

[c]*Institute of Physics, Bahauddin Zakariya University, Multan 60800, Pakistan. E-mail: dr.ehsan@bzu.edu.pk*

[d]*Civil Engineering Department NFC-IET, Multan, Pakistan*

[e]*Department of Chemistry, College of Science, Taif University, Taif, Saudi Arabia*

[f]*Department of Thermal Engineering and Industrial Facilities, Faculty of Mechanical Engineering, Opole University of Technology, ul. Prószkowska 76, 45-758 Opole, Poland*

[g]*Department of Physics, University of the Punjab, Lahore, Pakistan*

charging and discharging, excellent cycle stability, and environmental friendliness have garnered interest.[6,7] SCs are appealing due to their longer lifespan, which surpasses that of batteries, and they deliver more power than both regular capacitors and batteries.[8] They are an effective electrochemical energy storage device.[9] Their historical background started in the 1950s with the discovery of the electrochemical double-layer capacitor (EDLC), attributed to General Electric engineers. While researching fuel cells in 1961, Standard Oil of Ohio made an accidental discovery. In 1971, NEC named their device the "super-capacitor". In the meantime, Panasonic created the gold capacitor in 1978, and ELNA produced the Dyna-cap in 1987.[10–12] In a nutshell, SCs are categorized into three types: hybrid, double-layer, and pseudo-capacitors. The electrodes in hybrid capacitors are made from two different materials, which increases the capacitance and extends the voltage window.[5]

Regarding electrode materials, metal selenides with typical two-dimensional structures such as $MoSe_2$, CoSe, and $SnSe_2$ are very promising anode materials for high-performance applications because of their diverse compositions, simple synthesis methods, high theoretical specific capacitance, and good conductivity.[13] Transition metal selenides have been identified as potential electrode materials for supercapacitors, offering high energy densities and excellent rate performance.[3] ZnSe is considered one of the most promising anode materials owing to its impressive performance in various energy storage devices.[14] Ongoing advancements in semiconductors further highlight ZnSe as an important II–VI semiconductor, characterized by a bulk band gap of 2.67 eV and excellent optical transmission properties in the wavelength range from 0.5 to 22 μm,[15–20] along with a significant exciton binding energy of 21 meV and a Bohr radius of 3.8 nm.[21–23] It appears as a pale-yellow binary solid chemical. Therefore, it is a vital crystalline material for various applications and studies because of its quantum size effects and high surface atom percentage.[18] Additionally, it is chemically inert, non-hygroscopic, highly pure, densely structured, and easy to handle, making it an excellent material.[24]

Various methods, such as solid-state synthesis, co-precipitation, green synthesis, and chemical reduction, have been used to develop it.[13,25] Additionally, other techniques, such as melt quenching, aqueous colloidal methods, sonochemical methods, vapor-phase synthesis, and microwave irradiation, are employed to synthesize ZnSe.[26] However, the hydrothermal method is considered the most effective because of its many advantages over the others, including simplicity, phase purity, uniformity, and better control over synthesis conditions.[27] It features a crystal structure with an $F\bar{4}3m$ space group, an FCC symmetry, and lattice parameters of a, 1/4 b, 1/4 c, and 5.668 Å. Pyramidal [$ZnSe_4$] units are arranged in separate vertex-sharing chains, forming tunnel structures that are ideal for storing Li, Na, and K ions along the [110] direction.[13]

To enhance the supercapacitive performance of transition metal selenides, incorporating transition metal impurities (such as Al, Ag, Cu, Ni, and Co) as dopants is more effective than doping with rare earth ions.[28] Generally, host materials with a certain atomic weight percentage of transition metal ions replace cation sites in the ZnSe lattice. Nickel is particularly suitable as a dopant because the atomic radius difference between nickel(II) and Zn^{2+} is only 8.3%, making nickel(II) an ideal choice for doping in Zn-based semiconductor compounds. Consequently, Ni^{2+} atoms can replace Zn^{2+} atoms in the lattice. Additionally, since Zn^{2+} (0.74 Å) and Ni^{2+} (0.69 Å) have similar valence states and radii, Ni^{2+} may also substitute Zn^{2+} in the ZnSe lattice.[29] Incorporating transition metals into ZnSe matrices notably alters their electrical and electrochemical properties, leading us to select Ni/ZnSe semiconductors. As a result, Ni-doped ZnSe particles with sizes of 5 nm and 20 nm prepared at different temperatures exhibit a phase transition from cubic zinc blende to hexagonal wurtzite with increasing temperature.[23,30] The cubic phase is generally considered more stable than the hexagonal phase.[31]

Notably, ZnSe, a metal selenide, has been studied as a potential electrode material because of its impressive performance in energy storage devices. Comparing ZnSe to ZnO and ZnS, in particular, shows its higher electrochemical activity and electrical conductivity.[32] Regarding the rate performance of batteries and SCs, these materials have attracted considerable attention. As a result, developing efficient electrode materials for SCs and batteries remains a significant challenge.[33–35] Furthermore, incorporating Ni into ZnSe may be an optimal choice for enhancing ion transport properties and conductivity, as ZnSe has a wider band gap that can be reduced through Ni doping, which promotes conductivity. Additionally, Ni doping can induce lattice distortions that help improve electron and ion mobility, along with enhancing pseudocapacitive characteristics. This combination is relatively better than NiO and $NiSe_2$ owing to its optimal conductivity and stable matrix with Ni sites, which accommodate redox-active sites.

Primarily, when ZnSe is used as an anode material, it tends to pulverize and amorphize during charge and discharge cycles, leading to poor cycling stability. To address these issues, constructing a ZnSe/carbon hybrid material is considered one of the most effective ways to enhance the electrochemical performance of electrodes. ZnSe exhibits a significant synergistic effect with carbon, which greatly increases the anode's capacity for energy storage. Dispersing ZnSe nanoparticles in reduced graphene oxides to synthesize ZnSe–rGO nanocomposites as anode materials has been explored for all types of SCs.[13,14] Owing to its buffer effect and the 2D conducting channel, the unique structure of the three-dimensional porous graphene network offers high conductivity, rapid ion insertion, ample active sites, short diffusion paths for ions, and structural stability. Graphene and its analogs, such as rGO and GO, can be produced. Thanks to its structure, graphene shows excellent mechanical strength, flexibility, and high charge carrier mobility.[36–43] A published report has demonstrated that ZnSe–NiSe composites can deliver a specific capacity as high as 651.5 mAh g^{-1} at 1 A g^{-1} with an excellent cyclability of 98.7% after 10 000 cycles, yielding an energy density of 44.4 Wh kg^{-1}. These results suggest that ZnSe is a promising electrode material because of its relatively high capacity.[44]

Here, we systematically report the unique composition of ZnSe with 10% Ni and 10% rGO contents. The samples were prepared *via* a hydrothermal method, and ZnSe composites

with 2D material (rGO), were investigated. The prepared composites were used to investigate samples for electron and ion transport properties in high-performance energy storage SC applications. For instance, the ionic conductivity and the cation transference number were separately investigated for the optimized electrode series in a three-electrode assembly, which also demonstrated enhanced charge-transfer kinetics (rate constant), favorable exchange current density, and improved diffusion dynamics.

2. Materials and methods

To obtain graphene oxide (GO), a high-purity graphite powder was oxidized using the modified Hummers' method. In this process, 24 mL of H_2SO_4 and 4 mL of $NaNO_3$ in a volume ratio of 1 : 6 were carefully combined in a 180 mL beaker and stirred continuously in an ice bath for 50 minutes. Then, 1 g of the graphite powder was added while stirring vigorously, resulting in a black suspension. Next, 1.30 g of $KMnO_4$ was added to the suspension, which was then stirred continuously for 3 hours while maintaining the temperature around 15 °C. Afterward, 20 mL of DI water was gradually added while raising the temperature to approximately 45 °C to initiate the oxidation reaction. A dark brown solution was formed, indicating the creation of GO. Additionally, 5 mL of H_2O_2 was slowly added to decompose excess $KMnO_4$, followed by washing the mixture with 5% HCl to remove unreacted metal ions. The final product was obtained after centrifuging at 400 rpm for 15 minutes and then drying, resulting in the GO powder.

A simple solvothermal method was used to produce rGO by reducing GO sheets. First, 45 mL of absolute ethanol was added to an aqueous GO dispersion of 2 mg mL^{-1}. This solution was calcined at 180 °C for 3 hours and then sonicated and stirred continuously for 2 hours and 3 hours at 60 °C, respectively. Additionally, this suspension was placed in a Teflon-coated stainless-steel autoclave, which helped reduce GO sheets, and it was heated at about 180 °C for 3 hours. After cooling the autoclave to room temperature, the product was washed, dried, and obtained as a fine dark powder.

The procedure for preparing $Zn_{0.90}Ni_{0.10}Se$/rGO, was developed according to the described rationale, based on its stoichiometric composition. For example, ZnSe, which was selected as the electrode material, belonged to the chalcogenide family with a general formula AX, where A is any transition metal and X is a chalcogen such as Se or S. In this formula, doping Zn with Ni acted as a bimetallic to enhance electrical and electrochemical properties. The synthesized phase was physically mixed with rGO to reach an optimal weight percentage. The compound $Zn_{0.90}Ni_{0.10}Se$/rGO, containing 90% Ni-doped ZnSe (10% Ni and 90% Zn combined with Se in a total ratio of 1 : 1) and 10% rGO, was achieved *via* a hydrothermal synthesis route developed based on this approach.

First, the hydrothermal method was used to synthesize ZnSe. Then, 2.18 g of the selenium powder and 1.422 g of zinc acetate were each mixed in separate 20 mL beakers containing deionized water and stirred with a glass rod for 1 minute. The zinc acetate solution and selenium powder were placed on a magnetic stirrer, and a NaOH solution was added drop-wise while stirring to reach a pH of 8. Subsequently, the mixture was transferred to Teflon cylinders, which were then placed in an autoclave and heated in an oven at 160 °C for 4 hours. After cooling to room temperature, the reaction mixture was centrifuged at 2000 rpm for 10 minutes and washed several times with deionized water, followed by thorough rinsing with absolute ethanol. The washed samples were dried under vacuum at 100 °C for 2 hours and then annealed at 400 °C for approximately 3 hours. The resulting solution was dried to obtain a fine powder. This powder was mixed with 10% nickel nitrate

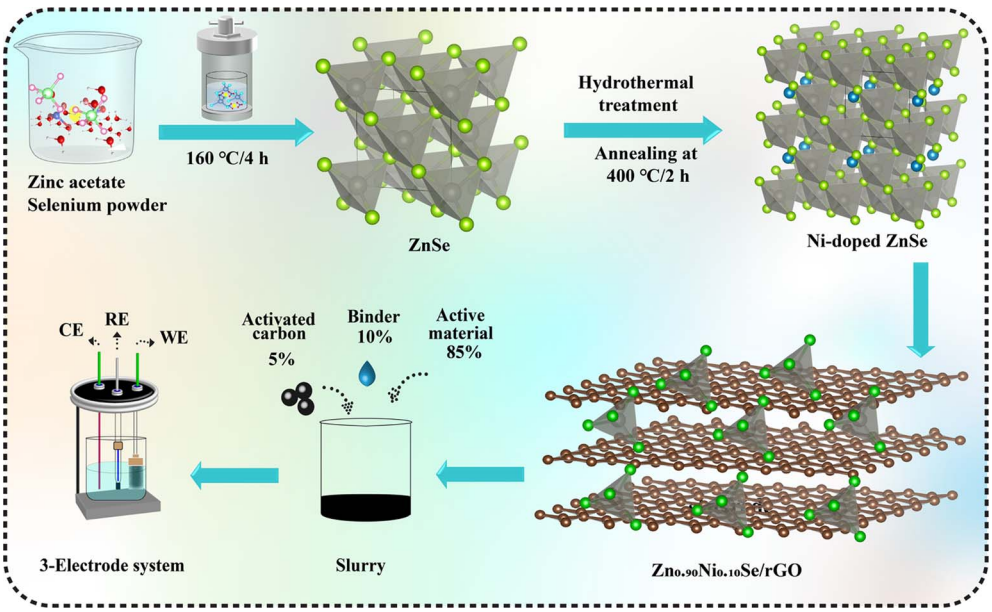

Fig. 1 Schematic profile of the sample's synthesis and electrochemical analysis.

($Ni(NO_3)_2$) to develop the dopant composition and stirred continuously to produce a homogeneous mixture, following the same method and conditions as those used for ZnSe synthesis. A similar process was used to prepare the composite recipes. The same procedure was applied to prepare the composites ZnSe/rGO and $Zn_{0.90}Ni_{0.10}Se$/rGO, in which rGO was included at 10%. The electrochemical analysis and material synthesis route are illustrated in Fig. 1.

A diffractometer was used to identify the crystal phases of the synthesized compounds with graphite-filtered Cu-K_α radiation (λ = 1.54 Å). Scanning electron microscopy (SEM) was conducted to examine the morphological features of ZnSe. The energy-dispersive X-ray spectroscopy (EDX) analysis of pure ZnSe confirmed the atomic and weight percentages of the elements, validating the stoichiometric composition of the samples.

3. Results and discussions

3.1 Structural analysis

Different sharp and broad peaks appear in the X-ray diffraction (XRD) patterns of all samples. For example, the analysis of ZnSe samples within the 2θ range from 20° to 100° was performed, as shown in Fig. 2(a–d). There are two crystal structures of ZnSe: one is the cubic blende structure, and the other is the hexagonal structure. The diffraction peaks of ZnSe are indexed according to ICSD #00-005-0522, indicating the cubic blende phase, while the hexagonal phase matches Entry No. 96-900-8880. The phase of Se_6 is associated with Entry No. 96-901-3139, as identified by the Match software for the undoped sample. The phase of ZnO corresponds to Match Entry No. 96-230-0451. The XRD data show fluctuations, with sharp and clearly defined peaks observed and indexed with the exact Miller indices (100), (111), (200), (220), (013), (311), (222), (202), (023), (400), (023), (331), (114), (015), (212), (024), (422), and (511), following the approach described by BD Cullity, confirming the presence of ZnSe. No additional peaks due to rGO inclusion in the composite recipe are observed in the XRD patterns, likely because of its amorphous nature and minimal concentration, as shown in Fig. 2(c and d). The crystal structure of ZnSe is displayed in Fig. 2(e), and the crystallite size variation is illustrated in Fig. 2(f).

Some additional peaks are observed in the XRD patterns with the doping of cations (Ni). These peaks might indicate the formation of secondary or impurity phases.[45] They suggest that excess Zn and Se oxides are present in the synthesized ZnSe powder. However, other peaks in the spectrum indicate the presence of impurities, making it difficult for ZnSe nanoparticles to form correctly and implying low purity. The peaks increase and become sharper as the temperature rises. For example, at 160 °C (a lower temperature), more unidentified peaks are observed, suggesting the poorer purity of the ZnSe at lower temperatures. This indicates that ZnSe's crystallinity significantly improves above 220 °C.[15,45] The residual zinc and SeO_2 contents in the powder decrease at a longer reaction time and a higher temperature.[20] In the spectrum, the (111) plane's XRD peak intensity appears to be higher than that of the others. As the Ni concentration increases, the XRD peak intensity also slightly increases. The peak at 2θ = 27.82° matches the development of ZnSe along the (111) crystal planes and suggests the strong distribution of the Ni dopant in the material.[47] The diffraction peaks of Ni-doped ZnSe show a slight shift to higher

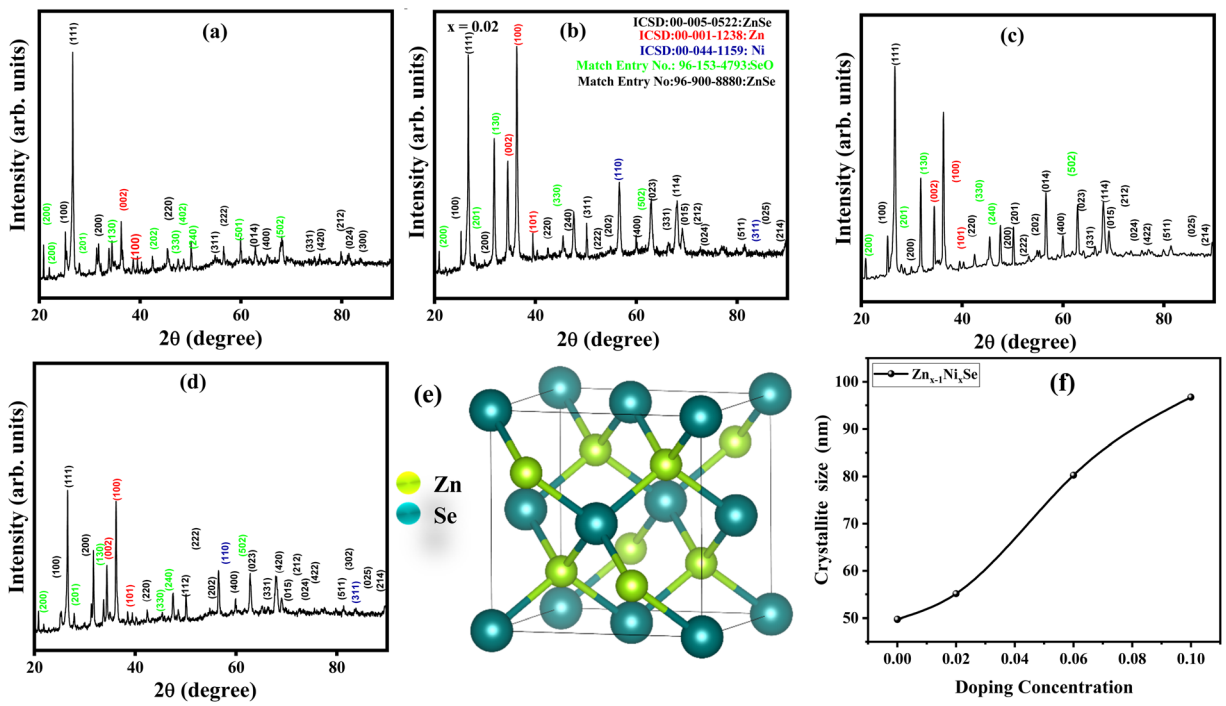

Fig. 2 (a) XRD patterns of ZnSe, (b) $Zn_{0.90}Ni_{0.10}Se$, (c) ZnSe/rGO, and (d) $Zn_{0.90}Ni_{0.10}Se$/rGO. (e) Crystal structure of ZnSe. (f) Crystallite size *vs.* different doping percentages.

angles with increasing Ni concentration (10% at the Zn site compared to pure ZnSe). This shift, caused by the (111) peak moving to a higher angle, results from divalent Ni atoms occupying Zn^{2+} sites, leading to a decrease in the interplanar spacing.[29]

The difference in cation ionic radii, which causes compressional stress in the host lattice, is responsible for the peak shift at very small angles. As the temperature rises, the powders exhibit a ZnSe hexagonal phase. The increasing temperature of the growing crystallite size enhances the kinetic energy of the metal ions and their rate of dissociation. Large-sized hexagonal phases crystallize as a byproduct in Ni-doped ZnSe due to the high kinetic energy of the reacting metal ions with mobilized Se^{2-} ions. Because of the aging process, the dopant ion (Ni^{2+}) initially attached to the ZnSe layer's surface diffuses into the lattice, resulting in a cubic structure and lattice formation. Initially, ZnSe is rapidly nucleated by rising temperatures; once stable, ZnSe nuclei form, and they act as catalysts for the addition of new ZnSe nuclei. This accelerates crystal growth and leads to the formation of a hexagonal structure.[23] Therefore, the substitution of transition metals, based on their atomic radii and infrared (IR) reflectivity, provides deeper insight into the system, allowing us to trace structural distortions caused by the doping element.[48] Match software was used to collect various data, such as the peak angles, interplanar spacings, peak heights, peak areas, and FWHMs of both pure and doped ZnSe samples at different percentages. The Scherrer formula was applied to determine the crystallite size.[45–50]

3.2 Morphological and elemental analysis

To gain a deeper understanding of the grain size distribution, shape, and size in each sample, a morphological survey was conducted using scanning electron microscopy (SEM). For example, the pristine sample (ZnSe), as shown in Fig. 3(a), has particles that are cylindrical, lacking sharp edges, and have nearly uniform sizes. Additionally, Fig. 3(b) shows that after the inclusion of Ni as a dopant, the texture of the microparticles enlarges while maintaining an uneven, wool-like shape, and the rod-like grain structures disappear.[31] The particles have an average diameter of 0.366 μm. As shown in Fig. 3(c), ZnSe is combined with rGO as a substitute, resulting in an uneven, rod-like morphology wrapped in wool-like clusters along with many tiny particles and pores. The grain size in this sample is estimated to be approximately 0.538 μm. The samples were annealed for about 3 hours at 400 °C. As a result, larger grains are developed, as shown in Fig. 2(a) and (b). The effects of the annealing time on the grain size and morphology of ZnSe nanoparticles are shown, with particles exhibiting both small and large grain sizes.[21]

Furthermore, to improve the electrochemical performance of ZnSe and $Zn_{0.90}Ni_{0.10}Se$, two composites were developed, namely, ZnSe/rGO and $Zn_{0.90}Ni_{0.10}Se$/rGO, respectively, aiming to enhance further ion transport properties in the Ni-doped ZnSe-based material. The primary objective of creating these two composites was to assess their potential for balanced electronic and ionic conduction in energy storage applications. In this context, morphological features play a key role, as shown in Fig. 3(c) and (d). It is evident that adding rGO significantly changes the morphology of pristine ZnSe and its highest Ni-doped version. Specifically, ZnSe/rGO displays different structures, including sheets clustered with nanoparticles that resemble bulk forms. The development of porous networks and wool-like flakes notably reduces these features. During electrochemical testing, the $Zn_{0.90}Ni_{0.10}Se$/rGO shows markedly improved rate performance, thanks to its accessible conductive networks, compared to all other samples.[51–55]

Besides this, the porosity factor, which promotes conductive channels, is a key element in enhancing the electrochemical properties of energy storage devices. For example, in brief, the ZnSe exhibits an ice cube-like morphology, offering more redox

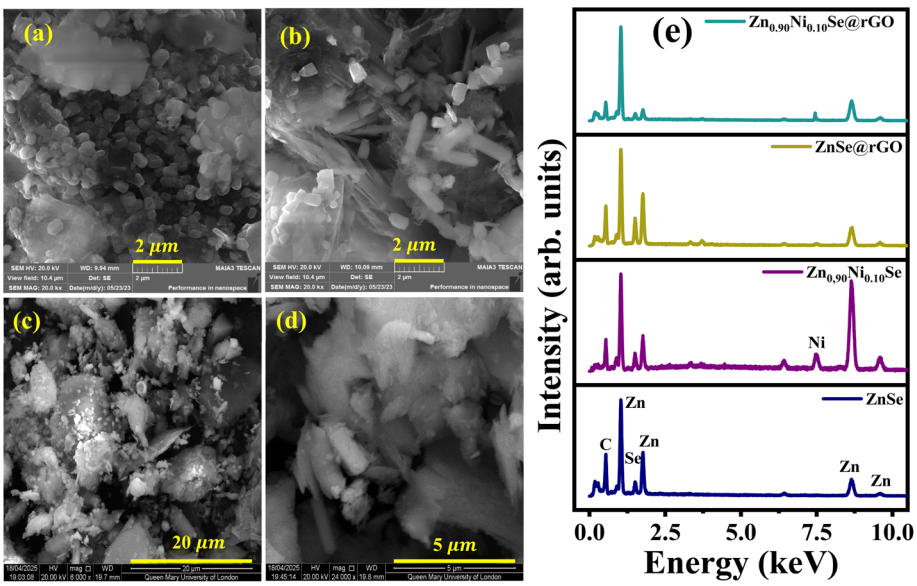

Fig. 3 (a–d) SEM images of ZnSe, $Zn_{0.90}Ni_{0.10}Se$, ZnSe/rGO, and $Zn_{0.90}Ni_{0.10}Se$/rGO. (e) EDX spectra of all samples.

Table 1 Elemental composition of ZnSe, $Zn_{0.90}Ni_{0.10}Se$, ZnSe/rGO, and $Zn_{0.90}Ni_{0.10}Se$/rGO

Sample	Wt% Zn	Wt% Se	Wt% Ni	Wt% C
ZnSe	45.29	54.71	0	0
$Zn_{0.90}Ni_{0.10}Se$	40.96	54.95	4.09	0
ZnSe/rGO	40.77	49.23	0	10
$Zn_{0.90}Ni_{0.10}Se$/rGO	36.86	49.45	3.68	10

active sites, but with poor conductivity, which was further improved by doping with Ni and adding rGO. Therefore, it can be concluded that porosity is not the only factor affecting charge carrier mobility; electrical conductivity, which allows for more efficient power transfer, also plays a crucial role, in determining, ion transport and structural stability. Electrochemical testing further confirms that the composite materials, rather than the pristine samples, deliver superior energy storage capabilities.

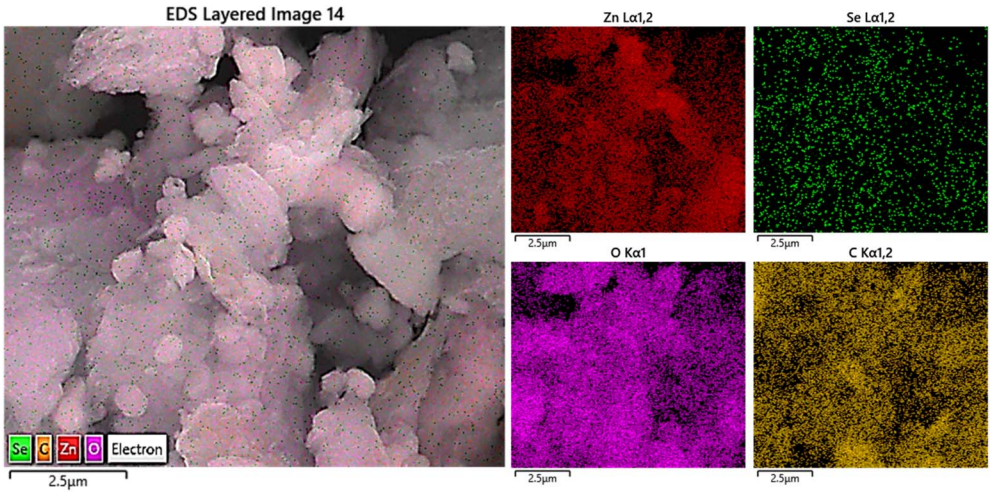

Fig. 4 Elemental mapping of ZnSe/rGO.

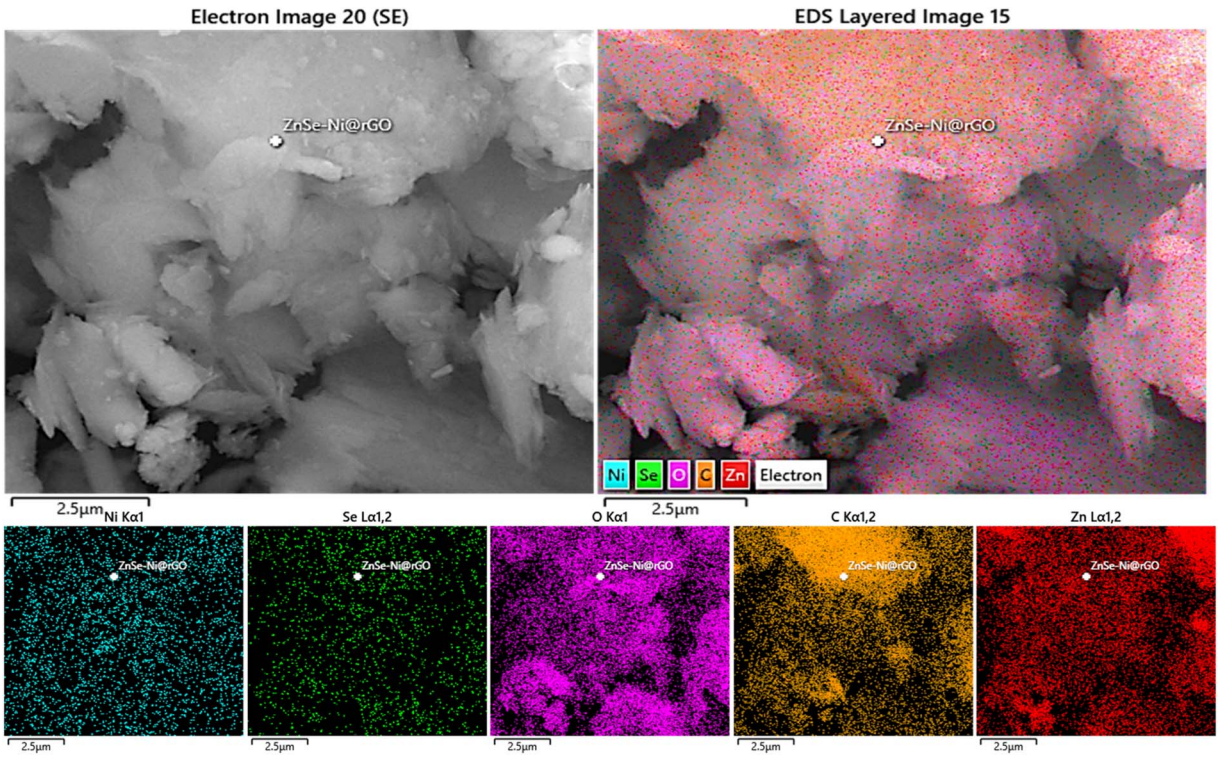

Fig. 5 Elemental mapping of $Zn_{0.90}Ni_{0.10}Se$/rGO.

The data analysis of the EDX patterns validates the stoichiometric composition of the elements in all samples. Zn is found to have three elemental peaks at 1.0, 9.6, and 8.6 keV, and Se has one at 1.6 keV; the O peak is seen at 1.5 keV. Ni has two peaks in doped samples located at 0.9 and 7.5 keV. Also, the essential elements in the composite samples, such as Zn, Se, and C in ZnSe/rGO and Zn, Ni, Se, C, and O in $Zn_{0.90}Ni_{0.10}Se$/rGO, as evidenced from the EDX spectra of all samples, are displayed in Fig. 3(e). The atomic weight percentage of each constituent is listed in Table 1.

Further justification is provided by the presentation of elemental mapping, which indicates the distribution of specific elements in ZnSe/rGO and $Zn_{0.90}Ni_{0.10}Se$/rGO, as shown in Fig. 4 and 5, respectively. For example, the distribution of Zn, Se, C, and O in ZnSe/rGO is represented by red, green, magenta, and orange colors, respectively. A similar pattern, including the Ni content in $Zn_{0.90}Ni_{0.10}Se$/rGO, is shown in Fig. 5 with different colors. These elemental maps confirm the presence and distribution of all essential elements in the composite samples within certain regions when analyzed using this technique.

3.3 Raman spectroscopy

Raman spectroscopy is a widely used non-destructive technique for detecting the stretching and vibrational modes, defects, and phase composition of a sample when monochromatic light interacts with a material's molecules. These features are typically observed at specific Raman shifts in the spectra. For example, the presence of any carbonaceous compound is confirmed by the G and D bands associated with the graphitic structure and disorderedness, which correspond to the defects present. In our case, the Raman spectra shown in Fig. 6 were obtained in the range from 200 to 2000 cm^{-1}, showing peaks at 563.81, 787.67, and 1117.39 cm^{-1}, corresponding to stretching and vibrational modes related to ZnSe/rGO and Ni-doped ZnSe/rGO. Specifically, the presence of rGO in the composite samples has been verified using the D band at 1374.05 and the G band at 1567.82 cm^{-1}, indicating the disorder and hybridized state of carbon. This survey not only validates the purity phase but also comprehends the information from stretching/vibration modes to G and D bands in the prepared samples.

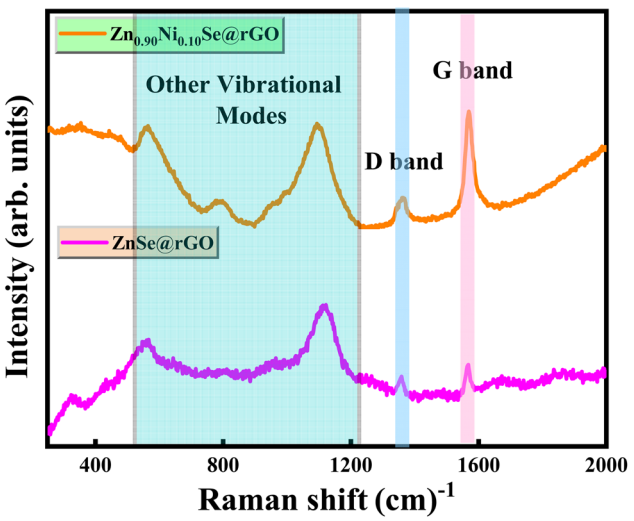

Fig. 6 Raman analysis of ZnSe/rGO and $Zn_{0.90}Ni_{0.10}Se$/rGO.

4. Electrochemical characterization

A typical three-electrode setup was used to examine the electrochemical properties of the resulting fabricated materials. The reference electrode was a silver/silver chloride (Ag/AgCl)-based electrode, while the counter electrode was a platinum (Pt) wire. The electrolyte medium consisted of an aqueous solution of 3 M potassium hydroxide (KOH), which was used to investigate the electrochemical behavior and charge–discharge kinetics by employing cyclic voltammetry (CV) measurements in the potential window from 0.0 V to 0.6 V *vs.* Ag/AgCl at a variety of scan rates (SRs), and galvanostatic charge–discharge (GCD) tests were conducted at current densities from 1 to 10 A g^{-1}. The internal (electrolyte) resistance charge-transfer dynamics and ion diffusion characteristics were measured at the electrode–electrolyte interface and in solution using electrochemical impedance spectroscopy (EIS) studies conducted over the wide frequency range from 10^{-2} Hz to 10^{5} Hz.

4.1 Electrochemical analysis

CV is a crucial technique for studying the redox behavior, electrochemical stability, and charge-transfer kinetics of materials. By adjusting the applied potential and SR, researchers can analyze the relationship between the potential changes and response current associated with redox reactions. For this purpose, CV measurements were performed between 0 and 0.6 V at SRs ranging from 5 to 100 mV s^{-1} for all fabricated electrodes (Fig. 7(a–d)). Thus, analyzing the dependence on the SR, peak potential, and peak current reveals that different potentials and SRs offer essential insights into the redox reaction kinetics, capacitance properties, and electron transfer mechanisms. The faradaic pseudo-capacitance is distinguished from the non-faradaic electric double-layer capacitance by the presence of clear redox peaks in cyclic voltammograms. As the SR decreases, the rGO-based ZnSe exhibits a quasi-rectangular CV characteristic of pseudocapacitive behavior. Furthermore, the prominent anodic and cathodic peaks become broader and more intense with increasing SRs, indicating the development of reversible faradaic pseudo-capacitance. A shift from surface-controlled to diffusion-limited kinetics is also observed in the power-law and peak-separation behavior, emphasizing the increasing role of redox processes in charge storage.

The redox peak current and CV area of $Zn_{0.90}Ni_{0.10}Se$ compared to the ZnSe electrode indicate that the addition of Ni leads to faster reaction kinetics, as evident from the integral area of the CV, which measures the specific capacitance values of the electroactive material. ZnSe and $Zn_{0.90}Ni_{0.10}Se$ electrodes exhibit the maximum specific capacitance values of 346.8 F g^{-1} and 1172.6 F g^{-1}, respectively, at a SR of 5 mV s^{-1}. This indicates that nickel in selenides is more electrochemically active

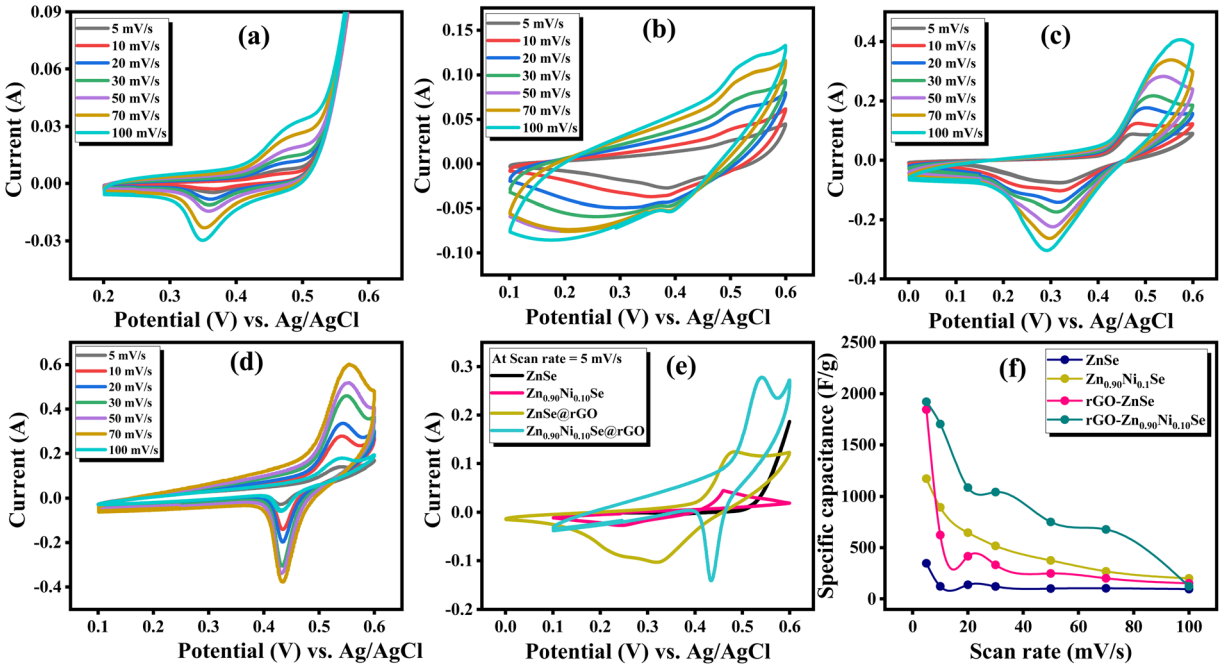

Fig. 7 CV curves at different scan rates for (a) ZnSe, (b) $Zn_{0.90}Ni_{0.10}Se$, (c) ZnSe/rGO, and (d) $Zn_{0.90}Ni_{0.10}Se$/rGO. (e) Combined CV curves at 5 mV s^{-1}, and (f) scan rate *vs.* specific capacitance.

than zinc and has the longest GCD curve discharging time due to the synergistic effect between Ni and ZnSe, which signifies its higher energy storage capacity. The specific capacitance values of ZnSe/rGO and $Zn_{0.90}Ni_{0.10}Se$/rGO electrodes at 5 mV s^{-1} are 1843.7 F g^{-1} and 1920.5 F g^{-1}, respectively, as determined from the CV curves. The composites with rGO show higher specific capacitance values than ZnSe and $Zn_{0.90}Ni_{0.10}Se$, respectively. The $Zn_{0.90}Ni_{0.10}Se$/rGO electrode demonstrates the highest specific capacitance among the ZnSe, ZnSe/rGO, and $Zn_{0.90}Ni_{0.10}Se$ electrodes. This electrode exhibits more optimal capacitive behavior due to its high SSA and superior electrochemical activity. The combined voltammograms for all samples, recorded at the lowest SR of 5 mV s^{-1}, are shown in Fig. 7(e). The purpose of this plot is to provide better insights into the electron transfer kinetics. Eqn (1) allows us to calculate each sample's capacitance (C_{sp}) based on the previous discussion of the observed redox peaks.

$$C_{sp} = \frac{\int_{V_i}^{V_f} I\,dV}{mv\Delta V} \quad (1)$$

The integral of the CV curve $\int_{V_i}^{V_f} I dV$ corresponds to the charge stored (area under the curve), while product mv is the active mass, and SR, in this instance. Table 2 provides the C_{sp} values for all samples, and Fig. 7(f) illustrates them. Compared to ZnSe-based electrode materials, this table shows that $Zn_{0.90}Ni_{0.10}Se$/rGO-based electrode materials possess the highest C_{sp} value ever achieved, which is approximately 1920.20 F g^{-1}. This reflects the superior potential of these electrode materials for hybrid capacitor technology.

Capacitive and diffusive contributions using Cottrell's equations and Dunn's equations are computed by employing the equations below.

$$i_{peak} = av^b \text{ or } \log(i_{peak}) = b\log(v) + \log(a) \quad (2)$$

$$I(v) = k_1 v + k_2 v^{1/2} \quad (3)$$

$$\frac{i_{peak}}{v^{0.5}} = k_1 v^{0.5} + k_2 \quad (4)$$

The values of anodic and cathodic peak currents and capacitive and diffusive contributions of each sample were computed using eqn (2)–(4), and their graphical representation is illustrated in Fig. 8(a–f). These graphs suggest the mixed

Table 2 Specific capacitance of ZnSe, $Zn_{0.90}Ni_{0.10}Se$, ZnSe/rGO, and $Zn_{0.90}Ni_{0.10}Se$/rGO electrodes at different scan rates

Specific capacitances (F g^{-1})				
Scan rates (mV s^{-1})	ZnSe	$Zn_{0.90}Ni_{0.10}Se$	ZnSe/rGO	$Zn_{0.90}Ni_{0.10}Se$/rGO
5	346.82	1172.60	1843.75	1920.20
10	121.53	893.17	623.28	1702.91
20	136.97	645.43	415.78	1085.98
30	120.90	517.17	331.72	1042.27
50	99.81	374.67	248.18	750.53
70	102.96	268.84	201.18	677.49
100	94.62	200.43	151.90	122.32

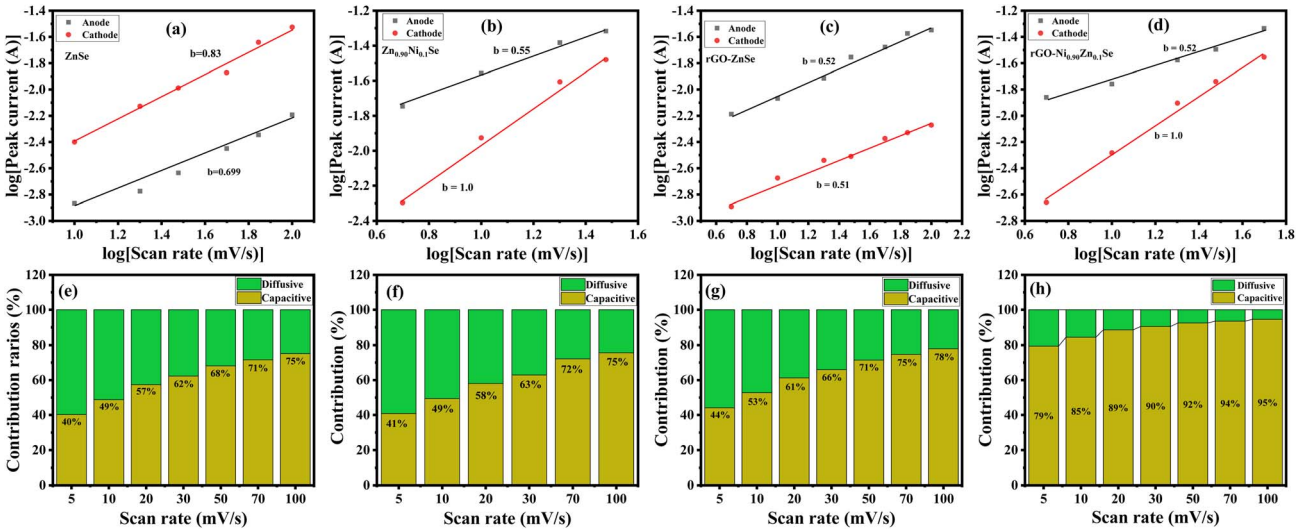

Fig. 8 (a–d) Values of b from the slope after the linear fitting of anodic and cathodic peak currents at multiple scan rates for all samples, and (e–h) capacitive and diffusive contributions at multiple scan rates for all samples.

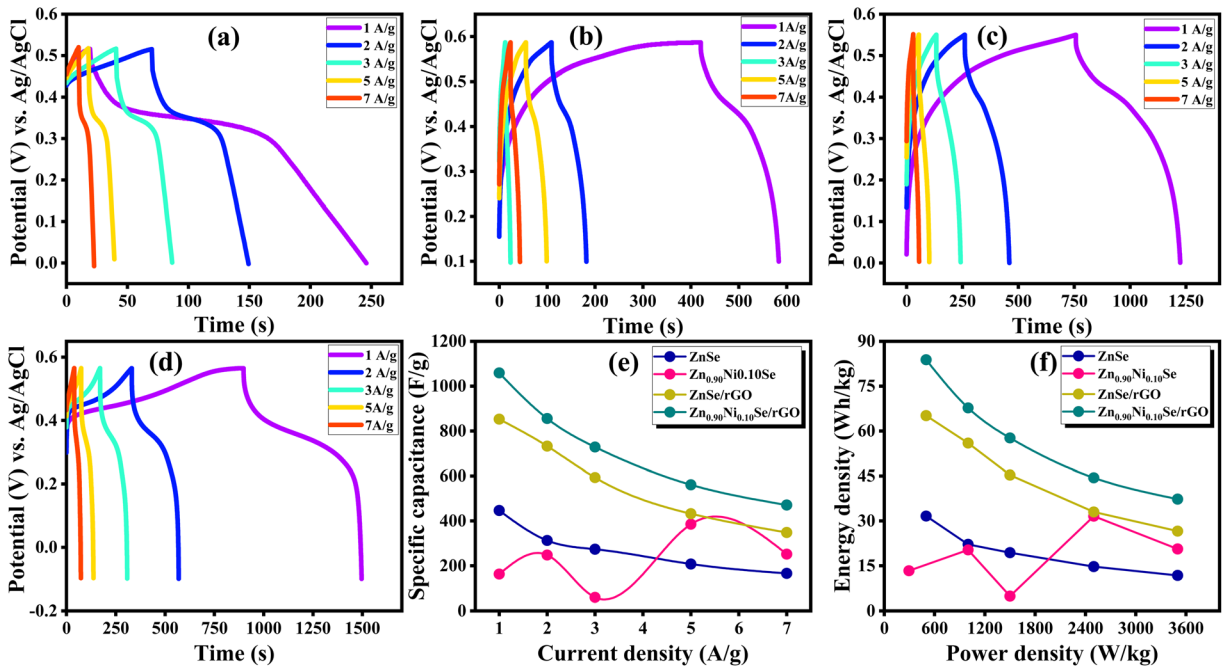

Fig. 9 (a–d) GCD curves of all samples, (e) current density *vs.* specific capacitance, and (f) Ragone plot.

contribution of surface-controlled and diffusion-controlled processes.

GCD tests were conducted to evaluate the electrochemical performance of all fabricated electrodes within the potential range of 0–0.6 V at current densities of 1–7 A g^{-1}. Fig. 9(a–d) displays the GCD profiles for each material. The redox behavior and pseudo-capacitance of the materials were identified using non-linear, plateau-like features in the GCD curves that matched the CV results. A higher accumulation of charges in both cases is indicated by a significant increase in the area under the GCD curve, which occurs because ions do not have enough time to enter the active material during high current density charging, as clearly shown in Fig. 9(a–d). Table 3 provides details about the changes in the observed specific capacitance for ZnSe/rGO electrodes. A clear positive trend is observed for the capacitance of the ZnSe/rGO electrodes with increasing rGO content and the impact of Ni doping. This improvement primarily results from the larger surface area provided by rGO, enabling better ion transport and increased exposure to active sites. Because rGO acts as a conducting scaffold, enhancing electrolyte penetration and facilitating fast redox reactions, key aspects of the pseudocapacitive behavior

Table 3 Discharge time, specific capacitance, energy density, and power density of ZnSe, $Zn_{0.90}Ni_{0.10}Se$, ZnSe/rGO, and $Zn_{0.90}Ni_{0.10}Se$/rGO

Sample	Current density (A g^{-1})	Discharge time (s)	Specific capacitance (F g^{-1})	Energy density (Wh kg^{-1})	Power density (W kg^{-1})
ZnSe	1	163.99	446.39	31.61	500
	2	73.88	312.78	22.15	1000
	3	9.69	273.70	19.38	1500
	5	44.64	207.74	14.71	2500
	7	19.11	166.07	11.76	3500
$Zn_{0.90}Ni_{0.10}Se$	1	226.60	162.96	13.35	295
	2	79.37	247.76	20.30	1000
	3	46.52	59.18	4.85	1500
	5	21.88	385.50	31.59	2500
	7	12.64	251.88	20.64	3500
ZnSe/rGO	1	466.89	852.50	65.12	500
	2	200.42	732.47	55.95	1000
	3	107.69	593.23	45.31	1500
	5	44.50	432.18	33.01	2500
	7	29.02	348.21	26.60	3500
$Zn_{0.90}Ni_{0.10}Se$/rGO	1	639.93	1058.75	83.81	500
	2	256.75	855.47	67.72	1000
	3	144.79	728.26	57.65	1500
	5	77.10	561.05	44.41	2500
	7	32.28	471.08	37.29	3500

are enhanced. The discharging time of the GCD curves gradually increases until it reaches the maximum. As a result, the rGO–$Zn_{0.90}Ni_{0.10}Se$ electrode exhibits the most significant area under the CV curve and the longest discharge time of the GCD curve, indicating superior energy storage capacity. Using eqn (5)–(7), the specific capacity was calculated at various current densities.

$$C_{sp} = \frac{I \times \Delta t}{m \times \Delta V} \quad (5)$$

$$E = \frac{V^2 \times C_{sp}}{3.6}\ \text{Wh kg}^{-1} \quad (6)$$

$$P = \frac{3600 \times E}{\Delta t}\ \text{W kg}^{-1} \quad (7)$$

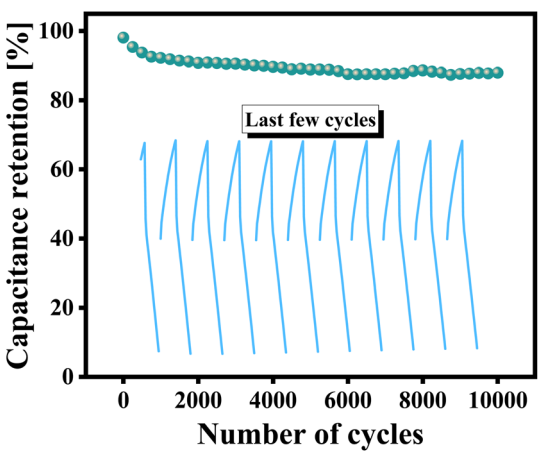

Fig. 10 Cyclic stability test of $Zn_{0.90}Ni_{0.10}Se$/rGO.

The active mass of the material is represented by m, the potential window by ΔV, the discharge time by Δt, and the current applied by I. The specific capacitance values of the $Zn_{0.90}Ni_{0.10}Se$/rGO electrode decrease steadily with increasing current density, dropping from 446.39, 162.96, 852.50, and 1058.75 F g^{-1} at 1 A g^{-1} to 166.07, 251.88, 348.21, and 471.08 at 7 A g^{-1}, respectively, supporting the previous discussion. The trends in the capacitance, energy density, and power density of each sample are shown in Fig. 9(e) and (f). Additionally, the non-linear charge/discharge curves of the rGO–$Zn_{0.90}Ni_{0.10}Se$ electrode align well with the CV redox peaks, showing 90.67% capacity retention after 10 000 cycles, which indicates excellent rate performance, improved cycling stability, and enhanced electrochemical activity, as shown in Fig. 10, illustrating how specific capacitance varies with the current density in the rGO-based Ni/ZnSe composite.

The specific capacitance for each sample decreases rapidly as the current density increases, likely due to the inherent resistance of the active materials and the inevitable rise in IR losses at higher current densities.[59,60] The power and energy densities of the rGO-based Ni/ZnSe composite were calculated *via* GCD testing using eqn (4) and (5). The highest energy densities for ZnSe, $Zn_{0.90}Ni_{0.10}Se$, ZnSe/rGO, and $Zn_{0.90}Ni_{0.10}Se$/rGO are 31.68, 13.35, 65.12, and 83.81 Wh kg^{-1}, respectively, at a current density of 1 A g^{-1}, while at 7 A g^{-1}, the energy densities are 11.76, 20.64, 26.60, and 37.29 Wh kg^{-1}, respectively. To distinguish the outcomes of this work, a comparison of different materials from a literature survey is reported in Table 4.[36,44,56–60] Interpreting the literature survey results, different electrode materials show varying lifespans and performance parameters. For example, the best ZnSe composite (ZnSe/$MoSe_2$) among all others demonstrates a cyclability of 99.96% after 5000 cycles, and ZnSe/FeSe has the highest capacitance (1419.8 W kg^{-1}) and energy density (63.20 Wh kg^{-1}) among all the reviewed

Table 4 Comparison of the electrochemical parameters of different ZnSe-based composites

Material	Specific capacitance ($F\ g^{-1}$)	Current density ($A\ g^{-1}$)	No. of cycles	Capacitance retention (%)	Energy density ($Wh\ kg^{-1}$)	Power density ($W\ kg^{-1}$)	Ref.
$ZnSe/CoSe_2$	645	1.0	5k	99.6	57	743	36
ZnSe/NiSe	651.5 mAh g^{-1}	1.0	10k	98.7	44.4	—	44
MnSe/ZnSe	1439.89	1	—	—	56.17	265	56
ZnSe/FeSe	1419.8	—	—	—	63.20	283.20	57
$ZnSe/MoSe_2$	450	1	2000	99.96%	43	740	58
NiSe	763.65 C g^{-1}	1.5	3000	83%	32.04	1112.4	59
$MnSe_2/CoSe_2$/rGO	1138 C g^{-1}	1	5000	80%	45.80	853.10	60
$Zn_{0.90}Ni_{0.10}Se$/rGO	1058.75	1	10 000	90.85%	83.81	500	This study

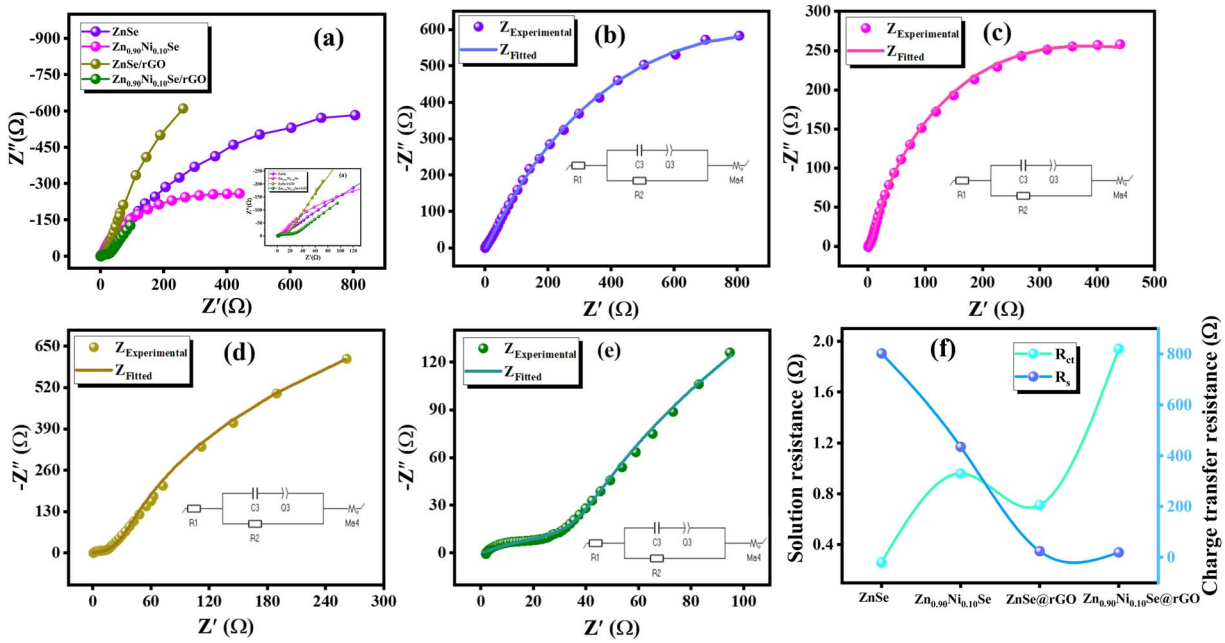

Fig. 11 (a) Combined EIS spectra of all samples, (b–e) fitting spectra of all samples, and (f) trend of solution and charge transfer resistances from sample to sample.

materials reported in Table 4, but it has the lowest energy density (83.81 Wh kg^{-1}) compared to this study. Our material exhibits the longest cycling period with an excellent stability of 90.86% after 10 000 GCD cycles, and it also shows outstanding energy density compared to others.

EIS was performed in a three-electrode setup to investigate the capacitive nature and ion kinetics of electrode materials. The EIS plots of rGO-based Ni/ZnSe composites are shown in Fig. 11(a) at an applied AC signal with an amplitude of 10 mA and in the frequency range from 10^{-2} Hz to 10^{5} Hz. For obtaining quantitative measurements, the fitting of Nyquist plots was performed using the equivalent circuit. With the help of similar circuits, one can study the electrical behavior of the circuit. A tiny semicircle is observed for the materials. Smaller semicircles indicate a significant improvement in conductivity, while larger semicircles indicate lower conductivity. The EIS plots of ZnSe-based nanocomposites show a semicircle with a smaller diameter. The diameter of the semicircle indicates the charge transfer resistance, which is directly correlated with conductivity and the contact developed at the electrode/electrolyte interface. The smaller the semicircle, the lower the charge transfer resistance.[59]

The composite electrodes ZnSe, $Zn_{0.90}Ni_{0.10}Se$, ZnSe/rGO, and $Zn_{0.90}Ni_{0.10}Se$/rGO exhibit the smallest semicircle diameter, indicating better charge transfer at the electrode/electrolyte interface. A similar circuit, shown in Fig. 11(b–e), illustrates how the internal resistance of the material, the binder resistance, and the ionic resistance of the electrolyte all contribute to the overall solution resistance (R_s). Charge transfer resistance (R_{ct}) is another value that affects at the electrode/electrolyte interface. Lower R_s and R_{ct} values indicate that rGO-based Ni/ZnSe electrodes, owing to their high SSAs and good electrochemical activity, exhibit more ideal capacitive behavior.[3] The impedance values of ZnSe, ZnSe/rGO, $Zn_{0.90}Ni_{0.10}Se$, and $Zn_{0.90}Ni_{0.10}Se$/rGO electrodes are listed in Tables 5 and 6, calculated using EC Lab Biologic Lab Software, yielding a 1% error margin estimated from the chi-square value. Here, the R_{ct} values of ZnSe and $Zn_{0.90}Ni_{0.10}Se$ are 802 Ω and 435 Ω,

Table 5 Values of elements for the corresponding fit circuit. $R_1 = R_s$, $R_2 = R_{ct}$, C_1 = capacitance, Q_1, Q_2 = constant-phase elements, W_1 = Warburg impedance, σ = ionic conductivity, and τ = relaxation time

Sample	R_1 (Ω) ± 1%	R_2 (Ω) ± 1%	C_1 (F) ± 1%	Q_1 ($Fs^{(a-1)}$) ± 1%	W_1 (Ω) ± 1%
ZnSe	0.26	802	0.0086	0.056	35.60
$Zn_{0.90}Ni_{0.10}Se$	0.96	435	0.76	0.008	9.77
ZnSe/rGO	0.71	23.89	0.45	0.001	0.68
$Zn_{0.90}Ni_{0.10}Se$/rGO	1.94	18.67	1.98	0.307	0.21

Table 6 Diffusion coefficients for ZnSe, $Zn_{0.90}Ni_{0.10}Se$, ZnSe/rGO, and $Zn_{0.90}Ni_{0.10}Se$/rGO

Sample	Ionic conductivity ($S\ cm^{-1}$) ± 1%	Transference number ± 1%	Rate constant ($cm\ s^{-1}$) ± 1%	Exchange current density ($A\ g^{-1}$) ± 1%	Diffusion coefficient ($m^2\ s^{-1}$) ± 1%
ZnSe	0.346	0.007	3.31×10^{-10}	3.2×10^{-5}	2.794×10^{-17}
$Zn_{0.90}Ni_{0.10}Se$	0.093	0.089	6.11×10^{-10}	5.9×10^{-5}	3.710×10^{-16}
ZnSe/rGO	0.126	0.510	1.11×10^{-8}	0.00107	7.658×10^{-14}
$Zn_{0.90}Ni_{0.10}Se$/rGO	0.037	0.902	1.42×10^{-8}	0.00137	8.030×10^{-13}

respectively. ZnSe has a much better R_{ct} than $Zn_{0.90}Ni_{0.10}Se$. Notably, the composite electrode $Zn_{0.90}Ni_{0.10}Se$ shows the lowest charge transfer resistance among the other electrodes, which can be attributed to its superior surface qualities and electrochemical activity. The addition of two-dimensional graphene improves the electronic conductivity of the material compared to the composite electrodes ZnSe/rGO and $Zn_{0.90}Ni_{0.10}Se$/rGO, whose resistance to the intercalation and de-intercalation of electrolyte ions is lower (R_{ct} = 23.89, 18.67 Ω), resulting in a higher rate of electrolyte ion transport to the active electrode surface. As a result, we observe a decrease in the solution and charge transfer resistances, as evidenced from the graph shown in Fig. 11(f). Consistent with the CV and GCD results, this increase enhances the number of conductive channels, thereby facilitating the movement of electrolyte ions. Therefore, graphene-based composites significantly boost the electrochemical performance of the electrode.

5. Ion transport properties

5.1 Diffusion coefficient

Quantifying ion diffusion is essential to understanding electrochemical performance. By calculating the diffusion coefficient of the synthesized materials from EIS, information about ion transport kinetics at the electrode–electrolyte interface was obtained. Better ionic mobility, as indicated by higher diffusion rates, is directly associated with increased rate capability and efficiency in devices such as supercapacitors and batteries.

The values of diffusion coefficients (D_{K^+}) of the fabricated electrodes with KOH as the electrolyte have been calculated using eqn (8).

$$D^{EIS}/K^+ = \frac{R^2T^2}{2 \times A^2 \times n^4 \times F^4 \times c^2 \times \delta^2} \quad (8)$$

Eqn (8) displays the diffusion coefficient for potassium ions in the KOH electrolyte, which is a quantitative measure of ionic transport within the electrode matrix. The product RT represents the gas constant and temperature, while A is the effective surface area of the electrode, and n, F, C, and σ denote the electron numbers, Faraday's constant, electrolyte concentration, and Warburg coefficient, respectively.[62,63] Table 6 presents the diffusion coefficients calculated from these values.

For instance, the diffusion coefficients are 2.79×10^{-17}, 3.71×10^{-16}, 7.65×10^{-14}, and 8.03×10^{-13} $m^2\ s^{-1}$ for ZnSe, $Zn_{0.90}Ni_{0.10}Se$, rGO–ZnSe, and rGO–$Zn_{0.90}Ni_{0.10}Se$, respectively. $Zn_{0.90}Ni_{0.10}Se$ exhibits the highest ion mobility among the samples, indicating greater diffusion kinetics and improved electrochemical performance. Table 6 illustrates the effect of the rGO concentration on ion transport. A lower Warburg factor indicates faster ion mobility, while a higher value suggests increased resistance and reduced diffusion. The diffusion coefficient reaches a value as high as 8.03×10^{-13} $m^2\ s^{-1}$ with a low Warburg value for the $Zn_{0.90}Ni_{0.10}Se$ sample, indicating efficient ion transport and potential for supercapacitor applications.

5.2 Ionic conductivity

Ionic conductivity plays a crucial role in the electrochemical efficiency of the electrode materials used in supercapacitor devices. Ionic conductivity directly affects the length and duration of the redox process, which are vital for charge storage. Materials with higher ionic conductivity enable faster ion movement and more efficient redox reactions, improving overall energy storage performance. Eqn (9) was employed in this research study to quantitatively measure ionic conductivity and facilitate an accurate assessment of the material's transport properties.

$$\sigma = \frac{L}{R_i \times A} \quad (9)$$

R_i is the ionic resistance, which correlates to solution resistance (R_s), while σ, A, and L are the ionic conductivity, surface area of electrodes, and thickness, respectively. Table 6 indicates that $Zn_{0.90}Ni_{0.1}Se$ has the highest ionic conductivity (0.346 S cm^{-1}), a level higher than that of ZnSe (0.093 S cm^{-1}), $Zn_{0.90}Ni_{0.1}Se$ (0.126 S cm^{-1}), and rGO–ZnSe (0.037 S cm^{-1}). This implies that $Zn_{0.90}Ni_{0.10}Se$ exhibits superior electrochemical performance and ion transport efficiency.

5.3 Transference number

The transference number is the ratio of the current carried by anions to that carried by cations in an electrolyte, representing their contributions to ionic conduction. It ranges between 0 and 1 and depends on the ionic size, polarization, defects, and temperature. Smaller ions tend to be more mobile, making a greater contribution to the current. Sorenson and Jacobsen's eqn (10) was employed to calculate the transference number in this research study.

$$t_+ = \frac{1}{1 + Z_d(0)/R_b} \tag{10}$$

Eqn (10) determines the cation transference number (t_+), in which (Z_d) is the Warburg impedance in the low-frequency region and (R_b) is the bulk electrolyte resistance. The anion transference number (t_-) is determined as t_+ ($t_- = 1 - t_+$). The t_+ values of ZnSe, $Zn_{0.90}Ni_{0.10}Se$, rGO–ZnSe, and rGO–$Zn_{0.90}Ni_{0.10}Se$ are 0.007, 0.089, 0.510, and 0.902, respectively, according to this equation. The findings unequivocally indicate that the incorporation of rGO reduces the anion transference number but increases the cation transference number. Such a shift signifies an enhancement in cation mobility within the electrolyte system. Table 6 indicates that the rGO–$Zn_{0.90}Ni_{0.10}$-Se-based electrode maintains the maximum cation contribution to the total current. This enhanced anion mobility provides evidence of more effective ionic transport, likely due to structural or interfacial modifications introduced by the incorporation of rGO.

5.4 Rate constant

The electrochemical reaction rate constant is indicative of the efficacy of charge carrier transport during the redox process. In the current research study, the charge transfer rates for ZnSe, $Zn_{0.90}Ni_{0.10}Se$, rGO–ZnSe, and rGO–$Zn_{0.90}Ni_{0.10}Se$ were calculated using eqn (11) from their charge transfer resistance values obtained *via* EIS analysis in a 1 M KOH electrolyte at an AC amplitude of 10 mA. These rate constants provide insights into the interfacial charge transport properties of each material.

$$\text{Rate constant} = \frac{RT}{F^2 \times R_{ct} \times C} \tag{11}$$

In this work, F represents Faraday's constant, *i.e.*, the electric charge per mole of electrons/ions, while R and T represent the universal gas constant and absolute room temperature, respectively. R_{ct} represents the EIS-measured charge transfer resistance, while C represents the concentration of electroactive species at the electrode–electrolyte interface. The Nernst equation (eqn (12)) may be utilized for determining the rate constant of an electrochemical process, provided that the proper calculation of C is performed. Using this relationship, an enhanced understanding of the interfacial processes that influence charge transfer efficiency in the electrode systems under study may be achieved.

$$E = E^0 + \frac{RT}{nF} \ln \frac{C_{surface}}{C_{bulk}} \tag{12}$$

The Nernst equation can be generalized and written in a more extended form as eqn (13).

$$C_{surface} = C_{bulk} \times e^{\left(\frac{nF\left(E-E^\circ\right)}{RT}\right)} \tag{13}$$

Here, $C_{surface}$ refers to the electrolyte species concentration at the electrode surface directly, while C_{bulk} refers to the bulk solution-phase concentration. The equation $E - E^\circ$ refers to the difference between the inherent standard potential of the redox pair and the external electrode potential. Furthermore, n indicates the number of electrons transported in the electrochemical reaction, F is Faraday's constant (96 485 C mol^{-1}), R is the universal gas constant (8.314 J mol^{-1-1} K^{-1}), and T is the absolute temperature in Kelvin, respectively.[65] Table 6 shows that the rGO–$Zn_{0.90}Ni_{0.10}Se$ electrode has the most significant rate constant (1.42×10^{-8} cm s^{-1}), indicating improved charge-transfer kinetics due to decreased interfacial resistance and increased electronic conductivity. However, the rGO/$Zn_{0.90}$-$Ni_{0.10}Se$ electrode has a slightly lower rate constant, indicating efficient but slower charge dynamics. Variations in the interfacial architecture and electron mobility are most likely to account for this disparity. The $Zn_{0.90}Ni_{0.10}Se$/rGO system has high potential due to its conductive network and the redox-active character of the bimetallic selenide.

Table 7 Comparison table of ion transport attributes of different materials

Sample	Ionic conductivity (S cm^{-1})	Transference number	Rate constant (cm s^{-1})	Exchange current density (mA g^{-1})	Diffusion coefficient (m^2 g^{-1})	Ref.
$LaNiO_3$/MXene	6.3×10^{-3}	0.3	—	—	9.5×10^{-13}	61
$BiMnO_3$/CNTs	0.978×10^{-3}	0.31	3.91×10^{-7}	—	3.45×10^{-18}	62
ZnO/CNTs	0.046	0.01	6.49×10^{-7}	—	3.69×10^{-12}	63
MoS_2/Se/CNTs	16.0×10^{-3}	0.35	0.0029	0.74	—	64
$BaCoO_3$/rGO	0.128	0.2	—	—	4.51×10^{-13}	65
$Zn_{0.90}Ni_{0.10}$/rGO	0.037	0.90	1.42×10^{-8}	0.000137	8.03×10^{-13}	This work

In summary, the ion transport properties discussed in this study have been thoroughly compared with the existing literature to support our findings. The variation in each transport parameter's fluctuation demonstrates how these characteristics differ across materials at their optimal concentrations. Therefore, this study, with the addition of these features, is much more comprehensive than simply reporting the electrochemical analysis limited to energy and power densities from CV and GCD analysis. The related studies from the literature are listed in Table 7.[61–65]

6. Conclusion

We successfully synthesized pure and Ni-doped ZnSe materials along with their composite with rGO. XRD analysis revealed multiphase crystalline materials. The crystallite size ranged from 49.72 nm to 96.74 nm, as estimated from XRD spectra. The size of particles increased as the Ni content increased. The electrochemical characterization of the $Zn_{0.90}Ni_{0.10}Se$/rGO composite exhibited the highest specific capacitance (1920.20 and 1058.75 F g^{-1}), significantly higher than that of pure ZnSe (346.8 and 446.39 F g^{-1}), as calculated from both CV and GCD curves at 5 mV s^{-1} and 1 A g^{-1}, respectively. Additionally, the rGO–$Zn_{0.90}Ni_{0.10}Se$ electrode exhibited excellent cycling stability (90.85% capacitance retention after 10 000 cycles) and a high specific power density of 3500 W kg^{-1} at a current density of 7 A g^{-1} and a high energy density (83.81 Wh kg^{-1}) at a current density of 1 A g^{-1}. Both Ni and rGO-doped composites exhibited a drop in their series and charge transfer resistances. Under optimal conditions, they showed excellent electrochemical performance, estimated from good ionic conductivity (0.037 S cm^{-1}), the highest transference number for cations (0.90), and a rate constant of 1.42×10^{-8} cm s^{-1} at an exchange current density of 0.00137 A g^{-1} and a diffusion coefficient value of 8.030×10^{-13} m^2 s^{-1}. Such a reasonable rate of performance for $Zn_{0.90}Ni_{0.10}Se$/rGO strongly suggests that it is the best electrode material for advanced energy storage applications.

Author contributions

Sana Ullah Asif: writing – original draft, formal analysis, data curation, conceptualization; Bushra Asghar: writing – original draft, formal analysis, data curation, conceptualization; Abdul Shakoor: writing – review & editing, visualization, methodology; Farooq Ahmad: writing – review & editing, visualization, supervision, project administration; Shahid Atiq: writing – review & editing, visualization, supervision, project administration; Abdul Waheed: validation, resources; Abdullah K. Alanazi: validation, resources, software; Muhammad Ehsan Mazhar: writing – review & editing, visualization, supervision, project administration; Muhammad Yahya Haroon; writing – review & editing, visualization; Sadia, writing – review & editing, visualization; Abdul Qayyum; writing – review & editing, visualization, supervision, project administration; Waseem Abbas, visualization, validation, software.

Conflicts of interest

There are no conflicts to declare.

Data availability

The data will be made available upon request.

Acknowledgements

The authors extend their appreciation to Taif University, Saudi Arabia, for supporting this work through the project number (TU-DSPP – 2024 – 16).

References

1 Y. Zhang, X. L. Huang, P. Tan, S. Bao, X. Zhang and M. Xu, Ultrafast kinetics and high capacity for Stable Sodium Storage enabled by Fe_3Se_4/ZnSe heterostructure engineering, *Composites, Part B*, 2021, **224**, 109166.
2 J. Libich, J. Máca, J. Vondrák, O. Čech and M. Sedlaříková, Supercapacitors: Properties and applications, *J. Energy Storage*, 2018, **17**, 224–227.
3 T. Shi, Z. Song, Y. Lv, D. Zhu, L. Miao, L. Gan, *et al.*, Hierarchical porous carbon guided by constructing organic-inorganic interpenetrating polymer networks to facilitate performance of zinc hybrid supercapacitors, *Chin. Chem. Lett.*, 2025, **36**(1), 109559.
4 P. Liu, Z. Song, Q. Huang, L. Miao, Y. Lv, L. Gan, *et al.*, Multi-H-bonded self-assembled superstructures for ultrahigh-capacity and ultralong-life all-organic ammonium-ion batteries, *Energy Environ. Sci.*, 2025, **18**(11), 5397–5406.
5 S. Jha, Y. Qin, Y. Chen, Z. Song, L. Miao, Y. Lv, *et al.*, Hydrogen-bond-guided micellar self-assembly-directed carbon superstructures for high-energy and ultralong-life zinc-ion hybrid capacitors, *J. Mater. Chem. A*, 2025, **13**(20), 15101–15110.
6 Z. Li, C. Ma, Y. Wen, Z. Wei, X. Xing, J. Chu, *et al.*, Highly conductive dodecaborate/MXene composites for high performance supercapacitors, *Nano Res.*, 2020, **13**(1), 196–202.
7 M. Pathak, D. Tamang, M. Kandasamy, B. Chakraborty and C. S. Rout, A comparative experimental and theoretical investigation on energy storage performance of $CoSe_2$, $NiSe_2$ and $MnSe_2$ nanostructures, *Appl. Mater. Today*, 2020, **19**, 100568.
8 W. Raza, F. Ali, N. Raza, Y. Luo, K. H. Kim, J. Yang, *et al.*, Recent advancements in supercapacitor technology, *Nano Energy*, 2018, **52**, 441–473.
9 J. Guo, Y. Zhao and T. Ma, Electrostatic self-assembly of 2D delaminated MXene (Ti_3C_2) onto Ni foam with superior electrochemical performance for supercapacitor, *Electrochim. Acta*, 2019, **305**, 164–174.
10 A. Iqbal, R. Nadeem, A. Shakoor, M. Luqman, M. Mehak, M. U. Salman, S. M. Ramay, F. Ahmad and S. Atiq, Enhanced ionic conductivity in synergistically developed $NiMnO_3$/CNTs nanocomposite electrode material in hybrid capacitors, *J. Energy Storage*, 2025, **134**(Part B), 118207.

11 A. Moftah and A. Al Shetiti, Review of supercapacitor technology, *Int. J. Comput. Sci. Electr. Electron.*, 2015, **3**(3), 226–231.
12 A. Namisnyk and J. Zhu, A survey of electrochemical supercapacitor technology, in *Australian Universities Power Engineering Conference*. University of Canterbury, New Zealand, 2003.
13 X. Cao, A. Li, Y. Yang and J. Chen, ZnSe nanoparticles dispersed in reduced graphene oxides with enhanced electrochemical properties in lithium/sodium ion batteries, *RSC Adv.*, 2018, **8**(45), 25734–25744.
14 P. Zhou, M. Zhang, L. Wang, Q. Huang, Z. Su, L. Li, *et al.*, Synthesis and electrochemical performance of ZnSe electrospinning nanofibers as an anode material for lithium ion and sodium ion batteries, *Front. Chem.*, 2019, **7**, 569.
15 X. Ren, Hydrothermal synthesis of ZnSe nanoparticle, in *2016 4th International Conference on Machinery, Materials and Computing Technology*, Atlantis Press, 2016, pp. 290–295.
16 H. K. Lee, Z. A. Talib, M. S. Mamat@ Mat Nazira, E. Wang, H. N. Lim, M. A. Mahdi, *et al.*, Effect of sodium hydroxide concentration in synthesizing zinc selenide/graphene oxide composite via microwave-assisted hydrothermal method, *Materials*, 2019, **12**(14), 2295.
17 F. Qiao, R. Kang, Q. Liang, Y. Cai, J. Bian and X. Hou, Tunability in the optical and electronic properties of ZnSe microspheres via Ag and Mn doping, *ACS Omega*, 2019, **4**(7), 12271–12277.
18 K. Ravindranadh, M. S. Shekhawat and M. C. Rao, Preparation and applications of ZnSe nanoparticles, in *AIP Conference Proceedings*, American Institute of Physics, 2013, pp. 219–220.
19 R. Sharma, S. L. Patel, S. Chander, M. D. Kannan and M. S. Dhaka, Physical properties of ZnSe thin films: Air and vacuum annealing evolution to buffer layer applications, *Phys. Lett. A*, 2020, **384**(4), 126097.
20 B. B. Wang and X. Z. Xu, Study on effects of time and temperature on growth of nanocrystalline zinc selenide synthesized by hydrothermal method, *J. Cryst. Growth*, 2009, **311**(23–24), 4759–4762.
21 B. T. T. Hien, N. T. Loan, P. T. Thuy and T. T. K. Chi, Annealing Time-Dependent Structural and Optical Properties of Znse Nanoparticles, *Res. Rev.*, 2018, **10**, 2321–6212.
22 K. Yadav, Y. Dwivedi and N. Jaggi, Structural and optical properties of Ni doped ZnSe nanoparticles, *J. Lumin.*, 2015, **158**, 181–187.
23 N. Priyadharsini, M. Elango, S. Vairam, T. Venkatachalam and M. Thamilselvan, Effect of temperature and pH on structural, optical and electrical properties of Ni doped ZnSe nanoparticles, *Optik*, 2016, **127**(19), 7543–7549.
24 A. R. Khataee, M. Hosseini, Y. Hanifehpour, M. Safarpour and S. W. Joo, Hydrothermal synthesis and characterization of Nd-doped ZnSe nanoparticles with enhanced visible light photocatalytic activity, *Res. Chem. Intermed.*, 2014, **40**(2), 495–508.
25 V. Beena, S. Ajitha, S. L. Rayar, C. Parvathiraja, K. Kannan and G. Palani, Enhanced photocatalytic and antibacterial activities of ZnSe nanoparticles, *J. Inorg. Organomet. Polym. Mater.*, 2021, **31**(11), 4390–4401.
26 G. Bhagavannarayana and M. A. Wahab, Structural, optical and electrical properties of ZnSe semiconductor nanoparticles, *Chalcogenide Lett.*, 2011, **8**(7), 435–440.
27 M. E. Mazhar, R. Asif, A. Waheed, J. Ahmad, M. N. Usmani, I. Syed, *et al.*, Electrochemical Sensing Of H_2o_2 By Hydrothermally Synthesized Pure Copper Oxide Materials, *Dig. J. Nanomater. Biostruct.*, 2020, **15**(4), 1239–1245.
28 I. Ahmad, M. E. Mazhar, M. N. Usmani, K. Khan, S. Ahmad and J. Ahmad, Auto-Combustion Facile Synthesis And Photocatalytic Hydrogen Evolution Activity Of Al And Ni Co-Doped Zno Nanoparticles, *J. Ovonic Res.*, 2019, **15**(1), 1.
29 D. Subramanyam, B. Hymavathi and B. R. Kumar, Synthesis and structural characterization of Ni doped ZnSe nanoparticles, *Int. J. Sci. Tech. Adv.*, 2019, **5**(2), 7–10.
30 S. M. Saini and K. S. Ojha, Optical and vibrational properties of Ni doped ZnSe nanospheres, *Optik*, 2021, **232**, 166570.
31 B. C. N. Obitte, I. L. Ikhioya, G. M. Whyte, U. K. Chime, B. A. Ezekoye, A. B. C. Ekwealor, *et al.*, The effects of doping and temperature on properties of electrochemically deposited Er^{3+} doped ZnSe thin films, *Opt. Mater.*, 2022, **124**, 111979.
32 F. Kong, J. Zheng, J. Chen, X. Li, S. Tao and B. Qian, The lithium ion storage performance of ZnSe particles with stable electrochemical reaction interfaces improved by carbon coating, *J. Phys. Chem. Solids*, 2021, **152**, 109987.
33 M. Hussain, B. M. Alotaibi, A. W. Alrowaily, H. A. Alyousef, M. F. Alotiby, M. Abdullah, *et al.*, Synthesis of high-performance supercapacitor electrode materials by hydrothermal route based on ZnSe/MnSe composite, *J. Phys. Chem. Solids*, 2024, **188**, 111919.
34 X. Xu, B. Mai, Z. Liu, S. Ji, R. Hu, L. Ouyang, *et al.*, Self-sacrificial template-directed ZnSe@ C as high performance anode for potassium-ion batteries, *Chem. Eng. J.*, 2020, **387**, 124061.
35 J. Chu, W. A. Wang, Q. Yu, C. Y. Lao, L. Zhang, K. Xi, *et al.*, Open ZnSe/C nanocages: multi-hierarchy stress-buffer for boosting cycling stability in potassium-ion batteries, *J. Mater. Chem. A*, 2020, **8**(2), 779–788.
36 M. Sangeetha Vidhya, R. Yuvakkumar and G. Ravi, Construction of bimetallic ZnSe–$CoSe_2$ flower as a finely tuned electrode for enhancing supercapacitor performance, *Int. J. Energy Res.*, 2022, **46**, 19894–19906.
37 P. Solís-Fernández, M. Bissett and H. Ago, Synthesis, structure and applications of graphene-based 2D heterostructures, *Chem. Soc. Rev.*, 2017, **46**(15), 4572–4613.
38 P. Forouzandeh and S. C. Pillai, MXenes-based nanocomposites for supercapacitor applications, *Curr. Opin. Chem. Eng.*, 2021, **33**, 100710.
39 A. Ausavasukhi, T. Siriphala, W. Limphirat and S. Nilmoung, *J. Met., Mater. Miner.*, 2024, **34**, 1–10.
40 I. Technology, P. Campus and N. Pathom, Biomass-based nitrogen-doped carbon/polyaniline composite as electrode material for supercapacitor devices, *J. Met., Mater. Miner.*, 2023, **33**, 1–11.

41 N. M. Thazin, N. Chaiammart, M. M. Thu and G. Panomsuwan, Effect of pre-carbonization temperature on the porous structure and electrochemical properties of activated carbon fibers derived from kapok for supercapacitor applications, *J. Met., Mater. Miner.*, 2022, **32**, 55–64.

42 N. Keawploy, R. Venkatkarthick, P. Wangyao and J. Qin, Screen printed textile electrodes using graphene and carbon nanotubes with silver for flexible supercapacitor applications, *J. Met., Mater. Miner.*, 2020, **30**, 39–44.

43 C. Tang, X. Wei, X. Cai, Q. An, P. Hu, J. Sheng, *et al.*, ZnSe microsphere/multiwalled carbon nanotube composites as high-rate and long-life anodes for sodium-ion batteries, *ACS Appl. Mater. Interfaces*, 2018, **10**(23), 19626–19632.

44 B. Ye, X. Cao, Q. Zhao and J. Wang, Coelectrodeposition of NiSe/ZnSe hybrid nanostructures as a battery-type electrode for an asymmetric supercapacitor, *J. Phys. Chem. C*, 2020, **124**, 21242–21249.

45 H. Y. Lin, J. D. Wei, C. C. Ou, J. W. Lu, C. Y. Tsai and M. H. Lee, Hydrothermal synthesis and characterization of mesoporous zinc selenide agglomerates by nitrogen bubble templates, *J. Alloys Compd.*, 2011, **509**(25), 7009–7015.

46 J. Ahmad, M. Qadeer Awan, R. Yasmin, M. Sabir, S. Anwar, M. Ehsan Mazhar, *et al.*, Infrared reflectance spectroscopy of $MgAl_2O_4$ nanoparticles substituted by K+ ions, *Int. J. Mod. Phys. B*, 2018, **32**(06), 1850067.

47 I. Ahmad, M. E. Mazhar, M. N. Usmani, M. Mehmood, W. Abbas, N. Akhtar, *et al.*, Auto-combustion synthesis of pure and Er, Dy co-doped ZnO nanomaterials for efficient methyl orange degradation using solar and visible light photocatalysis, *Mater. Res. Express*, 2019, **6**(7), 75044.

48 M. E. Mazhar, M. U. Tahir, J. Ahmad, Q. T. Ain, G. F. B. Solre, K. Qadir, *et al.*, Hydrothermally Synthesized Pure and Mn-Doped ZnS/ZnO Nanoparticles as Potential Candidate in Capacitive Devices, *J. Electron. Mater.*, 2023, **52**(12), 7962–7971.

49 M. E. Mazhar, S. Bakhtawar, A. M. Rana, M. N. Usmani, N. Akhtar, W. Abbas, *et al.*, Insight into the structural characterization of pure and Zr-doped hydrothermally synthesized cerium oxide nanoparticles, *Mater. Res. Express*, 2019, **6**(10), 105022.

50 E. J. W. Verwey and J. H. de Boer, Cation arrangement in a few oxides with crystal structures of the spinel type, *Recl. Trav. Chim. Pays-Bas*, 1936, **55**(6), 531–540.

51 H. M. Khan, S. Mumtaz, A. Waheed, J. Ahmad, M. E. Mazhar, W. Abbas, *et al.*, Enhanced structural and electrical properties of Ca-Ba rare earth substituted M-type hexaferrites, *J. Ovonic Res.*, 2021, **17**(2), 165.

52 H. M. Khan, Z. Mirrani, A. Waheed, J. Ahmad, M. E. Mazhar, M. N. Usmani, *et al.*, Synthesis and characterization of rare earth substituted M-type (Sr-Ba) hexaferrites, *J. Ovonic Res.*, 2020, **16**(5), 281–291.

53 J. Ahmad, M. Q. Awan, M. E. Mazhar and M. N. Ashiq, Effect of substitution of Co^{2+} ions on the structural and electrical properties of nanosized magnesium aluminate, *Phys. B*, 2011, **406**(2), 254–258.

54 G. Rahman, W. Nawab, W. Zazai, S. Bilal and S. A. Mian, Exploring the structural and charge storage properties of Ni–ZnS/ZnO composite synthesized by one-pot wet chemical route, *Mater. Chem. Phys.*, 2020, **252**, 123203.

55 B. Ye, X. Cao, Q. Zhao and J. Wang, Coelectrodeposition of NiSe/ZnSe hybrid nanostructures as a battery-type electrode for an asymmetric supercapacitor, *J. Phys. Chem. C*, 2020, **124**(39), 21242–21249.

56 M. Hussain, B. M. Alotaibi, A. W. Alrowaily, H. A. Alyousef, M. F. Alotiby, M. Abdullah, *et al.*, Synthesis of high-performance supercapacitor electrode materials by hydrothermal route based on ZnSe/MnSe composite, *J. Phys. Chem. Solids*, 2024, **188**, 111919.

57 T. Zahra, M. M. Alanazi, S. D. Alahmari, S. A. M. Abdelmohsen, M. Abdullah, S. Aman, *et al.*, Hydrothermally synthesized ZnSe@FeSe nanocomposite: a promising candidate for energy storage devices, *Int. J. Hydrogen Energy*, 2024, **59**, 97–106.

58 M. Sangeetha Vidhya, R. Yuvakkumar, P. Senthil Kumar, G. Ravi, D. Velauthapillai and M. Bijad, Recent progression of flower like ZnSe@$MoSe_2$ designed as an electrocatalyst for enhanced supercapacitor performance, *Top. Catal.*, 2022, **65**(5), 684–693.

59 S. M. Bekhit, S. G. Mohamed, I. M. Ghayad, S. Y. Attia, W. Metwally, R. Abdel-Karim, *et al.*, Snow crystal-like structure of NiSe as a binder-free electrode for high-performance hybrid supercapacitor, *J. Mater. Sci.*, 2022, **57**(22), 9955–9970.

60 H. Xuan, G. Zhang, X. Han, R. Wang, X. Liang, Y. Li, *et al.*, Construction of $MnSe_2$/$CoSe_2$/reduced graphene oxide composites with enhanced electrochemical performance as the battery-like electrode for hybrid supercapacitors, *J. Alloys Compd.*, 2021, **863**, 158751.

61 A. Shakoor, M. Adnan, M. Luqman, M. Ahmed Khan, S. M. Ramay, F. Ahmad, *et al.*, Synergistic Improvements in Ionic Conductivity, Diffusion Dynamics, and Transference Numbers for $LaNiO_3$/MXene Supercapacitor Electrodes, *Batteries Supercaps*, 2025, 2500014.

62 S. Fatima, H. Raza, A. Shakoor, F. Saeed, M. Luqman, M. S. Akhtar, *et al.*, Microstructural tailoring for enhanced response of carbon nanotube-filled $BiMnO_3$ electrodes, *Mater. Chem. Phys.*, 2025, 131198.

63 A. Hussain, A. Tufail, A. Shakoor, M. Mehak, M. S. Akhtar, S. M. Ramay, *et al.*, Synergistically tailored ionic conduction and transport in ZnO/CNTs based electrodes with enhanced electrochemical efficiency in supercapacitors, *Electrochim. Acta*, 2025, 146736.

64 A. Shahzad, M. Saleem, A. Shakoor, F. Ahmad, S. Atiq, O. Munir, *et al.*, Investigating electrochemical properties in CNT-modified MoS_2/Se composites for supercapacitor electrodes, *J. Power Sources*, 2025, **656**, 238067.

65 M. Shahzad, F. Ahmad, M. Ibraheem, A. Shakoor, S. M. Ramay, M. R. Raza, *et al.*, Tuning diffusion coefficient, ionic conductivity, and transference number in rGO/$BaCoO_3$ electrode material for optimized supercapacitor energy storage, *RSC Adv.*, 2025, **15**(8), 6308–6323.